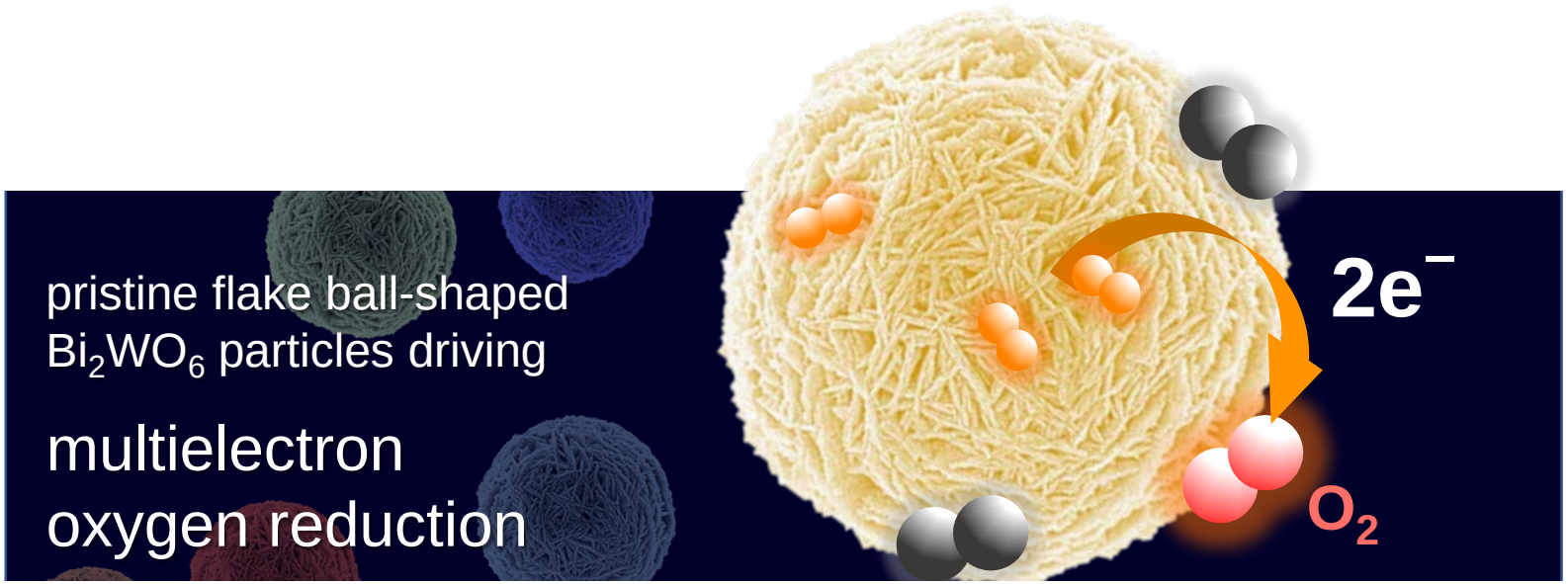
pristine flake ball-shaped
Bi_2WO_6 particles driving
multielectron
oxygen reduction
$2e^-$
O_2

Multielectron reduction of molecular oxygen in photocatalytic decomposition of organic compounds by bismuth tungstate particles without cocatalyst loading

Haruna Hori,[1] Mai Takashima,[1,2] Mai Takase,[3] Mika Kitamura,[1] Fumiaki Amano[4] and Bunsho Ohtani*[1,2]

[1]Graduate School of Environmental Science, Hokkaido University, Sapporo 060-0810, Japan
[2]Institute for Catalysis, Hokkaido University, Sapporo 001-0021, Japan
[3]Graduate School of Engineering, Muroran Institute of Technology, Muroran 050-8585, Japan
[4]Graduate School of Environmental Engineering, The University of Kitakyushu, Kitakyushu, 808-0135, Japan

Keywords photocatalytic organics decomposition; bismuth-tungstate flake ball-shaped particles; multielectron oxygen reduction; conduction band-bottom position; hydrogen peroxide

ABSTRACT

A photocatalytic reaction mechanism that involves multielectron reduction of molecular oxygen (O_2), as a key step, in photocatalytic decomposition of acetic acid by pristine bismuth tungstate (Bi_2WO_6; BWO) particles is proposed on the basis of results of studies on (i) comparison of photocatalytic activity trends of BWO, tungsten(VI) oxide and titanium(IV) oxide photocatalyst powders with or without platinum deposits in three photocatalytic reaction systems (oxidative decomposition of acetic acid in aerobic aqueous suspensions, methanol dehydrogenation in deaerated aqueous suspensions and O_2 liberation from deaerated silver salt solutions) and (ii) effects of morphology and structural properties of BWO particles on photocatalytic activities.

1. Introduction

There have been many practical applications of heterogeneous photocatalysis for oxidative decomposition and/or oxidation of inorganic and organic compounds, including microorganisms and viruses, in air or water [1-3]. Among the target materials, organic compounds can be mineralized, i.e., decomposed into carbon dioxide and water, through a mechanism that involves liberation of an organic radical species by positive holes in a photoabsorbing (photoexcited) photocatalyst or a hydroxyl radical produced by the reaction of a water molecule (hydroxyl group) and a positive hole, followed by radical chain reaction with peroxy radicals produced by the reaction of the initial organic radical and molecular oxygen (O_2) [4-8]. Considering such activity enhancement by the radical chain mechanism, the

*Corresponding author: (telephone) +81-11-706-9132, (facsimile) +81-11-706-9133, (email) ohtani@cat.hokudai.ac.jp (B. Ohtani)

overall efficiency of this photocatalytic organic decomposition (POD) has been reported to be high and quantum efficiency exceeding 100% was sometimes reported [9], even if the actual efficiency of utilization of photoexcited electron-positive hole pairs, i.e., intrinsic quantum efficiency, is very low. In this sense, the reported high efficiency of POD, especially using titanium(IV) oxide (titania), is attributable to this radical chain mechanism, not to the frequently suggested high oxidation ability of titania. This is supported by the fact that some metal-oxide photocatalysts, such as tungsten(VI) oxide (tungstena), exhibited very low or negligible photocatalytic activity for POD [10] even though the valence-band (VB) top position, i.e., the oxidation ability, of almost all metal oxides was expected to be the same as that suggested by Scaife [11]. Another example is the lower POD activity of rutile, one of the polymorphs of titania, which has been explained by its lower (more anodic) conduction-band (CB) bottom position [12]. Consequently, the parameter controlling the rate of POD might be efficiency of O_2 reduction by photoexcited electrons in the CB, which has not been emphasized in the literature [8]. For tungstena photocatalysts, it has been reported that loading of platinum (Pt) deposits on their surface dramatically enhances their POD activity, presumably through a mechanism that involves multielectron (probably two electrons) reduction of O_2 on the loaded Pt [10], and thus improvement in the efficiency of the O_2-reduction step is one of the effective strategies for enhancing POD activity of metal-oxide photocatalysts other than anatase titania.

As one of the potential photocatalysts exhibiting a high level of photocatalytic activity even under visible-light irradiation and stability under ultraviolet (UV) irradiation, bismuth tungstate (Bi_2WO_6; BWO) has attracted the attention of scientists in the field of photocatalysis. The group of the present authors developed a hydrothermal process for producing BWO particles with a characteristic flake ball (FB) structure [13] and proposed a non-Ostwald-ripening mechanism introducing the FB structure [14,15]. Although high levels of UV and visible-light POD activities of FB-BWO, even without a cocatalyst for O_2 reduction, have been reported [16], the present authors found that BWO cannot produce hydrogen (H_2) from aqueous methanol even when loaded with Pt deposits. Considering that titania photocatalysts can drive both POD and methanol dehydrogenation in bare and Pt-loaded forms, respectively, the above-mentioned behavior of BWO suggests that may suggest bare BWO particles drive POD through multielectron O_2 reduction like Pt-loaded tungstena photocatalysts, as was reported in the preceding communication [17]. The results of a detailed study on the photocatalytic activities of BWO and other bismuth-containing mixed metal oxides are presented in this paper.

2. Materials and Methods

2.1 Sample preparation

2.1.1 BWO samples

FB-BWO powder (sample FB) was prepared by hydrothermal reaction (HT) using a procedure reported previously [13-16,18,19]. A brief description of the procedure is as follows. A mixture of 5.0 mmol bismuth nitrate pentahydrate ($Bi(NO_3)_3 \cdot 5H_2O$; Wako Pure Chemical) and 2.75 mmol sodium tungstate dihydrate ($Na_2WO_4 \cdot 2H_2O$; Wako Pure Chemical) (W/Bi = 0.55) in 70 mL of water was poured in a sealed Teflon (PTFE) bottle with a stainless-steel outer bottle (San-ai Science HUT-100) and heated without agitation/stirring at 433 K for 20 h in an oven. After cooling to ambient temperature, the resultant slightly yellow product was washed with Milli-Q water and dried at 393 K in air.

Wet-milled samples (samples WML and WMH) were prepared with a Fritsch Pulverisette-7 planetary ball mill. A mixture of FB (1.8 g), zirconia beads (0.3 mm; 14.4 g) and Milli-Q water (8.0 mL) in a zirconia bottle (internal volume: 46.6 mL) was agitated at 500 rpm for 6 h. After separation of the zirconia beads by filtration, a suspension of the resultant solid in Milli-Q water was sonicated for 2 min by a YAMATO–Branson 5510 ultrasonic cleaner (42 kHz; 180 W), left to stand for 25 min at ambient temperature, and divided into two parts: the upper part (50 mL) containing relatively light particles (sample WML) and the lower precipitate part containing relatively heavy particles (sample WMH). Powdery forms of WML and WMH were collected by centrifugation at 3000 rpm for 30 min and drying in air at 393 K overnight.

A part of each BWO sample (samples FB, WML and WMH) was calcined in air at 773 for 3 h in an electric furnace to obtain samples 500FB, 500WML and 500WMH, respectively. A dry-milled sample of FB (sample DM) was prepared by manual braying 0.46 g of FB in an agate mortar for 2 h.

2.1.2 Reference samples

Four kinds of titania (Showa Denko Ceramics FP-6: sample FP-6, Evonik P25 (Nippon Aerosil): sample P25, Showa Denko Ceramics ST-G2: sample ST-G2, Tayca MT-150A: sample MT-150A) and two kinds of tungstena (Kojundo Chemical Laboratory: sample Kojundo and Aldrich: sample Aldrich) powder were used as received as reference samples in this study.

2.1.3 Pt loading

In a one-step photodeposition sequence, a 100-mg portion of a sample was suspended in 50vol% aqueous methanol (10 mL) containing hydrogen hexachloroplatinate(IV) hexahydrate (0.5 or 2.0wt% as metallic Pt) as a Pt source, and the resultant suspension was placed in a test tube and irradiated at > 290 nm under an argon atmosphere by a 400-W mercury

arc (Eiko-sha 400) for 80 min. The resultant Pt-loaded samples, generally gray or black in color, were collected, washed with Milli-Q water, and dried at 393 K.

In a two-step sequence, a 5.0-mL aqueous suspension of a 100-mg sample with the Pt source (2.0wt%) was first irradiated under air and irradiated again under an argon atmosphere after adding 5.0-mL 50vol% aqueous methanol. The Pt-loaded samples were recovered in a similar way.

2.2 Characterization of samples

2.2.1 Scanning electron microscopy

Scanning electron microscopic (SEM) images of samples were recorded on a JEOL JSM-7400M field emission-type scanning electron microscope in a mode of secondary-electron image (SEI) with operating conditions of 5.0–10.0-kV electron-acceleration voltage, 10.0-μA current and 3–6-mm working distance. A small portion of a powdery sample was placed on a brass sample stage (12 mm in diameter; 10 mm in height) covered with carbon tape (Okenshoji #15-1096) and evacuated (< 100 Pa) at ambient temperature overnight before measurement.

2.2.2 Specific surface area and pore-size distribution analyses

A sample (500 mg) evacuated at 473 K for 2 h as a pretreatment was used for measurement of nitrogen adsorption at 77 K on a Quantachrome (previously Yuasa Ionics) Autosorb-6 surface area and pore size analyzer. Specific surface area (SSA) was calculated from adsorption isotherms by the Brunauer–Emmett–Teller (BET) equation, and pore-size distribution was also estimated from the adsorption isotherms using Horvath–Kawazoe (HK) and Barrett–Joyner–Halenda (BJH) methods derived by assuming slit-type and cylinder-type pores, respectively.

2.2.3 X-Ray diffractometry

Composition and crystallinity of samples were analyzed by X-ray diffractometry using nickel(II) oxide (NiO; Wako Pure Chemical) as an internal crystalline standard [15,20]. In the standard procedure used in this study, 300 mg of a sample and 75 mg of NiO were mixed thoroughly in an agate mortar, and the X-ray diffraction (XRD) pattern of the mixture was recorded on a Rigaku SmartLab X-ray diffractometer (copper K_α radiation; 40 kV, 30 mA) with a scanning rate of 1.0º min^{-1} and steps of 0.008–0.02º in the 2θ range of 3–80º. Recorded diffractograms were analyzed using the software PDXL (Rigaku) including a RIETAN-FP Rietveld analysis package [21]. Crystallite size (D_{131}) was estimated by the Scherrer equation with corrected peak width of a 131 peak, i.e., crystallite size in the direction vertical to the (131) lattice plane was estimated. Since it is known that the flat surface of BWO plates is parallel to (010), the BWO-plate thickness (t_{BWO}) was roughly estimated by multiplying D_{131} by 0.82 based on the assumption that BWO was present only in the form of flat plates [16].

2.2.4 Diffuse-reflectance spectroscopy

Diffuse reflectance spectra of samples were measured by an ultraviolet and visible spectrophotometer (JASCO V-670) equipped with an integrating sphere unit PIN-757 for diffuse-reflectance measurement. Spectra in the wavelength range of 200–700 nm or 200–900 nm were recoded with a scanning rate of 200 nm min^{-1}, bandwidth of 5.0 nm and data uptake interval of 1.0 nm. Barium sulfate ($BaSO_4$) was used as a reference. In some measurements, the sample was diluted to 10% with $BaSO_4$.

2.3 Photocatalytic activity test

Three kinds of photocatalytic reaction systems were used for tests of photocatalytic activities of samples: (1) oxidative decomposition of acetic acid (POD) in aerobic aqueous solutions (CO_2 system; $CH_3COOH + 2O_2 \rightarrow 2CO_2 + 2H_2O$) [22-24], (2) dehydrogenation of methanol in deaerated aqueous solutions (H_2 system; $CH_3OH \rightarrow HCHO + H_2$) [25,26] and (3) silver-metal deposition along with O_2 liberation (O_2 system; $4Ag^+ + 2H_2O \rightarrow 4H^+ + 4Ag + O_2$) [27]. In the CO_2, H_2 and O_2 systems, 50 mg of a sample was suspended in 5.0-mL aerobic 5.0vol% aqueous acetic acid, deaerated 50vol% aqueous methanol and deaerated 0.050-mmol L^{-1} aqueous solution of silver fluoride, respectively, and irradiated by a 400-W mercury arc (Eiko-sha 400) with 1000-rpm magnetic stirring. Liberated CO_2, H_2 and O_2 in the gas phase of reaction tubes were analyzed by gas chromatography using a Shimadzu GC-8AIT equipped with a TCD and columns packed with Porapak-Q (for CO_2) and molecular sieve 5A (for H_2 and O_2). Photocatalytic activities were evaluated as the rates of liberation of those products.

2.4 Qualitative analysis of hydrogen peroxide

To a supernatant solution of a reaction mixture (CO_2 system) after photoirradiation was added ten drops of 30% aqueous solution of titanium(IV) sulfate (Wako Pure Chemical) to check the yellow color for detection of hydrogen peroxide. The detection limit is approximately few tens nanomoles in a 5.0-mL supernatant solution.

3. Results and Discussion

3.1 Morphology of BWO samples

Figure 1 shows SEM images of the BWO samples used in this study. FB particles as-prepared by HT of suspensions containing bismuth and tungsten components exhibited, as has been reported previously [14,15], a hierarchical structure (spherical assembly of flakes of stacked crystallite plates), while wet-milled samples WML and WMH had no such FB structure.

(Fig. 1)

It has been shown that an FB has a spherical inner void space that is produced during the course of HT synthesis [14,15]. As also seen in Fig. 1, calcination of samples led to the formation of

slightly densified particles (500FB, 500WML and 500WMH), as will be discussed in the following sections, without changing their basic morphologies.

3.2 Crystalline structure

Figure 2 summarizes XRD patterns of samples (taken without an internal standard NiO for clarity).

(Fig. 2)

All patterns of BWO samples coincided with that of authentic BWO, russellite (Bi_2WO_6; JCPDS card no. 39-0256), pattern [16], and no other peaks were observed. BWO-crystalline contents and BWO-plate thicknesses, as well as water (volatile compounds) contents, are listed in Table 1.

(Table 1)

The sample FB contained ca. 17% of non-crystalline (NC) components, including amorphous solids and water. Based on the assumption that all of the bismuth and tungsten components in the starting materials remained in the solid product, not reaction solutions and washings, and 5mol%-excess tungsten in the starting mixture remains as (amorphous) tungstic acid or (tungsten(IV) oxide monohydrate), minimally ca. 3% of 17% NC was attributed to tungstic acid. Then the remaining ca. 13% NC part (excluding ca. 1% water) might be amorphous BWO. The NC content was increased by wet milling to 25% and 19% in WML and WMH samples, respectively. The higher NC content in WML than in WMH is attributable to amorphous BWO in smaller particles and possible relatively high water content (not measured).

The thickness of BWO plates (t_{BWO}) estimated from crystallite size for uncalcined samples was ca. 12–14 nm, corresponding to ca. 70 layers of (010) planes, being consistent with the above-mentioned explanation of possible change by wet milling leading to disassembly of BWO plates and destruction of plates keeping their thickness. The thicknesses of WML and WMH samples were almost doubled by calcination (500WML and 500WMH), while only ca. 40-50% increase in the thickness of FB samples was observed. Since flakes in FB samples are composed of stacked plates, neighboring plates may be fused to thicker monocrystalline plates, leading to an increase in crystallite size D_{131} (and t_{BWO}), the thickness doubling for WML and WMH samples suggests that two plates, on average, are fused by calcination. For FB samples, however, fusion of BWO plates to yield thicker monocrystalline plates might be limited because the basal parts of plates are fixed so as not be able to adjust crystalline lattice matching with each other. This may cause the lower thickness ratio of ca. 1.5. This hypothesis is consistent with the above-discussed change in specific surface area and pore volume (estimated by the HK method) by calcination as discussed in the following sections.

3.3 Specific surface area of BWO samples

As has been reported [13], the extraordinarily high SSA of FB (Table 1), 20 $m^2\ g^{-1}$, for such micrometer-sized particles is attributable to the unique hieratic FB structure (Fig. 1), and

SSA of wet-milled samples (WML and WMH) was almost only doubled (42–43 $m^2 g^{-1}$). This indicates that flakes, stacked crystalline plates, in sample FB were disassembled into individual pieces, with slight reduction in size, by wet-milling. It should be noted that the change in SSA by calcination depended on the original particle morphology; 773-K calcination of FB induced negligible change in morphology as can be seen in Fig. 1, but its SSA was almost halved. Similarly, SSAs of samples WML and WMH became ca. one third by calcination. These SSA reductions are attributable to fusion of BWO plates that were separated (at least for nitrogen to be able to penetrate between plates) before calcination, being consistent with the proposed change in t_{BWO} in the preceding section.

3.4 Pore-size distribution in BWO samples

Figures 3(a) and 3(b) show pore-size distributions of samples calculated by the HK and BJH methods, respectively.

(Fig. 3)

The pore-size distribution estimated by the HK method assuming slit-type pores (Fig. 3(a)) seems to be consistent with the above-mentioned changes in flakes in BWO; there seems to be nanometer-sized spaces between BWO crystalline plates in the as-prepared FB sample and some of those spaces are closed by the fusion of plates when the sample was calcined (500FB), while wet milling of FB increases the pore (slit) volume by ca. two fold and calcination of milled samples decreases the volume by ca. one third, and those pore-volume ratios, 2 and 1/3, seem to be similar to the ratio of SSA changes (Table 1). On the other hand, pore-size distribution calculated by the BJH method (Fig. 3(b)) shows possible spaces between particles, i.e., interparticle spaces since the range of pore sizes is ca. three orders of magnification larger than that calculated by the HK method. In this case, the volumes remained almost constant with calcination for as-prepared FB and wet-milled samples (WML and WMH) but were increased by wet milling.

3.5 Pt-photodeposited BWO samples

SEM images of Pt-photodeposited BWO samples are shown in Fig. 4.

(Fig. 4)

Small particles in a size range of a few or several nanometers that were not observed in non-platinized samples are seen in all of the images, and any form of BWO could be platinized by photocatalytic deposition using hexachloroplatinic acid and methanol as a precursor of Pt and an electron donor, respectively [28]. Immediately after the commencement of photoirradiation, the color of the suspensions changed from light pale yellow to dark grey or black, indicating the formation of metallic Pt particles, but little evolution of hydrogen was detected in either the one-step or two-step deposition method, as is usually observed for deposition of Pt on titania particles. Different from the results for tungsten(VI) oxide [10], two-step deposition did not seem to give Pt deposits that are finer than those prepared through

one-step deposition, as far as seen in these SEM images, though there was still a possibility that there were very fine (below the detection limit of ca. 1 nm in FE-SEM images) Pt particles on the surface. Since there seems to be no effective way for proving definite contact between BWO and Pt deposits for electron transfer other than observation of hydrogen evolution during the course of photocatalytic deposition in the presence of electron donors, it is impossible to assume that Pt deposits are electrically isolated, i.e., there is no electron transfer between Pt deposits and BWO at all; at least some effective contact between them can be assumed on the basis of the above-described SEM observations.

3.6 Photoabsorption properties of BWO samples

Figure 5 (upper) shows the diffuse reflectance spectra of BWO samples.

(Fig. 5)

The upward shift of spectra at wavelengths > 500 nm might be caused by the possible difference in reflectivity of the sample and reference $BaSO_4$ and therefore might not be true photoabsorption. Although the absorption edge wavelength for all of the BWO samples was ca. 440 nm, corresponding to a 2.8-eV band gap, the spectrum curvature in the wavelength range of 350–450 nm of FB samples (FB and 500FB) was shifted upward, i.e., a shoulder existed, compared with those of milled samples. Figure 5 (lower) shows the diffuse reflectance spectra of BWO samples, including sample DM, diluted (10wt%) with $BaSO_4$. Although sample DM had no FB structure in its SEM image (data not shown), the DM spectrum still contained a shoulder after dry milling. Based on the assumption that dry milling destroyed the FB structure but did not change the composition of samples, the shoulder at ca. 400 nm is attributable to a component (components) removed by wet milling, not to structure-originating color such as optical confinement [29] or multiple reflection in stacked BWO crystalline layers. One of the most probable candidates for components that were removed is amorphous tungstena, which might be dissolved by wet milling.

On the basis of these considerations, wet milling might only slightly change the composition of FB but cause destruction of the FB structure, and optical properties, e.g., band-gap photoabsorption, therefore remained almost constant.

3.7 Photocatalytic activities of BWO and other metal oxides

Photocatalytic activities of the BWO samples were examined in three different photocatalytic reaction systems and compared with those of the other metal oxides, titania and tungstena (Fig. 6).

(Fig. 6)

In this study, we focused on the trends of the photocatalytic activities of metal oxides in the three systems, not on the absolute activities depending on the kind of metal oxide (For BWO, the structure-activity correlation will be discussed later.). Actually, titania photocatalysts

tended to exhibit higher photocatalytic activities than those of BWO and tungstena. In Fig. 6, the Y-axis for BWO and tungstena is therefore enlarged by five times.

A characteristic feature of BWO photocatalytic activity was negligible activity for methanol dehydrogenation (H_2 system) [30,31], similar to the trend of tungstena, and the actual rate of H_2 liberation by 2wt% Pt-loaded FB was 0.13 μmol h^{-1}. Because of the expected relatively high overpotential for H_2 liberation on the surfaces of metal oxides, at least for titania photocatalysts, it is well known and has been well documented that Pt loading is indispensable for driving photocatalytic H_2 liberation [25,32,33] by reducing the H_2 overpotential to almost zero. One of the possible reasons for this negligible BWO activity in the H_2 system is a poor or negligible effective electric contact between substantial Pt deposits and BWO-particle surfaces. However, as was discussed in the preceding section, it is not reasonable to assume a negligible effective electric contact for Pt deposits produced by reduction of the Pt precursor with photoexcited electrons in BWO (or tungstena) or the presence of completely insulating layers between the metal-oxide surfaces and Pt particles. Furthermore, POD-activity enhancement by Pt loading, as discussed later, supports possible electron transfer from BWO to Pt deposits. Therefore, it can be assumed that the potential of photoexcited electrons in BWO, i.e., potential of the CB bottom (CBB) of BWO, is lower than the standard electrode potential (SEP) of proton/hydrogen (0 V; SHE = $E(H^+/H_2)$), as has been shown for tungstena based on the results of platinization [10].

For oxygen liberation from aqueous silver-fluoride solutions (O_2 system), BWO samples, as well as tungstena samples, exhibited appreciable activities. Since it has been shown that the larger the size of titania photocatalyst particles is, the higher is the activity in the O_2 system and vice versa, as was seen for small-sized (ca. 13 nm) MT-150A titana particles [34,35], the higher activities of calcined BWO samples and commercial tungstena samples with large surface areas can be interpreted similarly. Therefore, the CBB of BWO must be higher than the SEP of silver ion/silver metal (0.80 V vs SHE), and this assumption is consistent with the fact that photodeposition of Pt proceeds on BWO (and tungstena) through the reduction of hexachloroplatinum(IV) ions with photoexcited electrons.

The above-mentioned trends were commonly observed for BWO and tungstena, but different trends were observed for acetic-acid decomposition (CO_2 system); the BWO samples showed photocatalytic activities that were higher than or comparable to those of titania samples, while the activities of tungstena samples were low and were enhanced to be a comparable level by Pt loading. As was reported previously [10], such a low level of tungstena activity is attributable to the tungstena CBB potential, which is lower than the SEP of one-electron reduction of oxygen, and enhancement of the activity by Pt loading is attributable to the catalytic action of Pt deposits enabling two-electron reduction of oxygen. It should be noted that BWO photocatalytic activities were also enhanced by Pt loading, and this fact supports the above-mentioned assumption that Pt deposits on BWO particles have electrical contact enabling transfer of electrons in BWO to the Pt deposits. However, the actual enhancement ratio, i.e.,

the ratio of activity of a platinized sample to that of a non-platinized sample, was smaller than 2 except for the case of 500FB (ca. 3) (The reason for this exception is discussed in the following section.), while the enhancement ratios for titania and tungstena samples were approximately 5.

3.8 POD activities of bare and platinized BWO samples

Figure 7 shows the photocatalytic activities of BWO samples with or without loaded Pt deposits for decomposition of acetic acid in aqueous suspensions under aerobic conditions (CO_2 system).

(Fig. 7)

Among the uncalcined bare samples, the activity of FB was the highest. One of the possible (and frequently stated) reasons is that wet milling induces the formation of amorphous (defective) layers, which may enhance the recombination of electrons and positive holes as well as disassembly of flakes in FB. The lower activity of milled samples recovered, or became even better than that of FB, by calcination, since the above-mentioned amorphous layers might be recrystallized. On the other hand, the activity of FB, which may be sufficiently crystallized during HT, was almost constant even after calcination.

The activities of bare BWO samples were improved due to the enhanced two-electron reduction process catalyzed by Pt deposits, but bare BWO samples may drive this two-electron oxygen reduction and thereby the enhancement ratios were not so high compared with the ratios for tungstena with poor two-electron reduction ability and titania with relatively high single-electron reduction ability. The enhancement ratios for BWO samples depended on the amount (data not shown) and on the conditions for Pt photodeposition (Fig. 7), and the differences in activities may be closely related to the density of Pt deposits and the contact between BWO surfaces and deposits. However, roughly speaking, the enhancement ratios for BWO samples were ca. 2 or less. This is consistent with the proposal that BWO can drive multielectron reduction of O_2. As described in the preceding section, an exception is the ratio for 500FB, which was slightly higher than 2. A possible explanation is as follows. As was indicated by the pore-volume analysis, there may be spaces between crystalline plates in flakes of uncalcined FB, and the calcination induces fusion of plates to give thicker plates in 500FB. Assuming negligible penetration of chloroplatinic acid and Pt deposition in the spaces in FB, only the outer plates could be platinized and the inner plates were left not-platinized, while for the calcined sample (500FB), platinization of the outer plates can activate the inner part since they are fused. This speculation means that the enhancement ratio of FB was underestimated. Similarly lower enhancement ratio (or negligible enhancement) of photocatalytic activity of uncalcined milled samples (WML and WMH) could be interpreted by the suggested amorphous (defective) layers on their surfaces that retard the electron transfer to Pt deposits.

3.9 Mechanism of O_2 reduction in BWO photocatalysis

The findings described above and previously reported results for POD activity of Pt-loaded tungstena lead to the mechanistic interpretation of bare-BWO POD activity with multielectron reduction of O_2 on BWO photocatalyst particles. The estimated band positions and related SEPs are shown in Fig. 8.

(Fig. 8)

In the H_2 system, in which protons (water) are reduced by photoexcited electrons, the fact that BWO shows negligible photocatalytic activity indicates that the CBB position of BWO (at pH = 0) is lower than the SHE ($E(H^+/H_2)$). Based on the assumption of a pH-dependent shift in the band position of metal oxides [36], the BWO CBB position is, at any pH, lower (more anodic) than $E(H^+/H_2)$. Then, assuming that the VB-top (VBT) position of BWO is the same as those of other metal oxides [11], such as anatase and rutile titania [12], and that the band gap of BWO is 2.8 eV, the BWO CBB is estimated to be 0.24 V, which is lower (more anodic) than $E(H^+/H_2)$ and consistent with the above-mentioned interpretation. On the other hand, CBB positions of anatase and rutile titania were estimated to be slightly higher (more cathodic) than $E(H^+/H_2)$ based on the results of statistical analysis of photocatalytic activities of titania samples [34,35], being consistent with the reported titania band positions [12]. For photocatalytic reactions involving O_2 reduction by photoexcited electrons, it is necessary to compare the CBBs with corresponding SEPs. There are two possible SEPs for one-electron O_2 reduction: (1) oxygen/hydroperoxy radical ($O_2 + H^+ + e^- = HO_2\bullet$, $E(O_2/HO_2\bullet) = -0.05$ V at pH=0) [37] and (2) oxygen/superoxide anion radical ($O_2 + e^- = O_2\bullet^-$, $E(O_2/O_2\bullet^-) = -0.28$ V) [37]. The rutile CBB position is estimated to be 0.04 V at pH = 0 [12], lower than $E(O_2/HO_2\bullet)$, and thereby one-electron oxygen reduction may not proceed. This is a possible explanation of the apparently lower photocatalytic activity of rutile than that of anatase when the POD activity test was performed under the conditions of pH lower than pK_a of hydroperoxy radical, 4.85 [38]. Since the CBB positions of BWO and tungstena are even lower than the rutile CBB position as shown in Fig. 8, one-electron O_2 reduction is not allowed in acidic (pH ca. 1) acetic-acid suspensions. Loading of cocatalysts for multielectron O_2 reduction such as Pt onto tungstena, therefore, enhances the POD activity [10]. On the other hand, BWO can drive POD without cocatalyst loading through multielectron reduction, though it cannot be concluded whether the number of electrons for O_2 reduction is two ($O_2 + 2H^+ + 2e^- = H_2O_2$, $E(O_2/H_2O_2) = 0.70$ V at pH = 0) [37] or four ($O_2 + 4H^+ + 4e^- = 2H_2O$, $E(O_2/H_2O) = 1.23$ V at pH = 0) [37], since SEPs of these processes are sufficiently lower (more anodic) than the BWO CBB.

There can be another interpretation (or other interpretations) for the appreciable POD activity of BWO having a lower CBB, e.g., one-electron O_2 reduction proceeds by electron transfer from the CBB to surface-adsorbed O_2, the potential of which is lowered by modification of the electronic structure due to adsorption on the BWO surface. It should be noted that it is scientifically impossible to exclude any possibilities other than the above-mentioned multielectron O_2 reduction mechanism.

The reason why BWO can drive multielectron O_2 reduction is unknown at present, but a preliminary study on photocatalytic activities of another bismuth tungstate and bismuth molybdates (Table 2) suggested that inclusion of a bismuth component may be a key for the multielectron O_2 reduction; similar photocatalytic-activity trends observed for $Bi_2W_2O_9$, Bi_2MoO_6, $Bi_2Mo_2O_9$ and $Bi_2Mo_3O_{12}$ particles exhibiting appreciable CO_2 (POD) activities but negligible H_2 activity suggest bismuth components in the tungstate and molybdates enable multielectron O_2 reduction [39].

(Table 2)

Another significant finding in the authors' preliminary study is that titania POD activity is markedly enhanced by deposition of bismuth-metal or oxide particles on the titania-particle surface, presumably due to induction of multielectron O_2 reduction [40]. Thus, it is expected that studies on catalytic functions of bismuth components/compounds will lead to novel strategies for the development of highly active photocatalysts for decomposition of organic/inorganic compounds in the presence of O_2.

3.10 Attempts for detection of hydrogen peroxide in POD by BWO

It is expected that hydrogen peroxide (H_2O_2) was liberated, at least as reaction intermediate, when two-electron O_2 reduction proceeds on BWO. In qualitative H_2O_2 detection experiments using titanium(IV) sulfate, a yellow color suggesting the liberation of H_2O_2 was observed when photoirradiated POD reaction mixtures containing FB, WML or WMH samples were examined. However, the estimated molar amount of H_2O_2 was maximally a few tens of nanomoles [41] and could be negligible compared with the amount of liberated CO_2.

It should be noted that the above-described results prove neither two-electron O_2 reduction nor one (or four) -electron O_2 reduction on BWO photocatalysts. (1) Even if two-electron O_2 reduction proceeds, the resultant H_2O_2 can be easily further reduced to water since the SEP for further reduction, $E(H_2O_2/H_2O)$ (1.78 V vs SHE) [37], is more anodic than $E(O_2/H_2O_2)$. Even if the produced H_2O_2 remains unreacted, the amount should be small compared to that of CO_2 liberation, since POD is accelerated by the radical chain mechanism in which the actual number of utilized positive holes (and excited electrons) is much smaller than that of the actual oxidized product [6]. (2) Even if only one-electron O_2 reduction takes place, H_2O_2 can be liberated by the following second electron transfer, i.e., detection of an appreciable amount of H_2O_2 cannot be proof excluding one-electron reduction. Thus, such product analysis or trapping experiments do not seem to be effective for proving the mechanism.

3.11 Structure-dependent POD activity of BWO samples

In the preceding section, POD activities of BWO samples were discussed; lower activities of wet-milled samples were attributed to the possible creation of crystalline defects, enhancing electron-positive hole recombination, by wet milling, and calcination might reduce

the defect density for recovery of POD activity. Similar trends were observed commonly in two reaction systems, CO_2 and O_2 systems, and seem reasonable since electron-hole recombination takes place commonly in photocatalytic reactions. However, considering that four positive holes are required for O_2 liberation in the O_2 system and assuming multielectron O_2 reduction in the CO_2 system when BWO is used as a photocatalyst, it is possible to interpret the photocatalytic-activity trends by assuming an effective size of particles for driving multielectron transfer that requires multiple-photon absorption. Since flakes, assemblies of crystalline BWO plates, were decomposed into small thin platelets by wet milling, the effective particle size was markedly decreased, resulting in much lower probability of multiphoton absorption by one particle of WML or WMH. While calcination of those wet-milled samples might reduce the density of detrimental crystalline defects, SSA was reduced to ca. one third, suggesting the fusion of thin small platelets to particles of larger effective size. Based on the results of statistical analysis, it has been suggested the titania photocatalytic activities in the O_2 system are mainly controlled by secondary particle size, i.e., size of aggregates of crystallites, presumably because O_2 liberation requires multiphoton absorption and positive holes can migrate within a particle aggregate. Therefore, it is expected that calcination-induced fusion of thin BWO platelets in WML and WMH increases the effective particle size for multielectron transfer. On the other hand, calcination of FB caused negligible morphological change and, thereby, photocatalytic activities were almost the same even after calcination.

On the basis of these considerations, the authors have performed preliminary kinetic studies including light-intensity dependence to obtain results being consistent with the above-proposed multielectron O_2 reduction mechanism, and the details will be published in the near future [42].

4. Conclusions

On the basis of the experimental results reported in this paper and previously reported results, it is proposed that pristine, i.e., non cocatalyst-loaded BWO photocatalyst particles, can drive efficient POD in an aqueous suspension through a mechanism involving multielectron O_2 reduction as a key reaction step. One of the significant findings is that it is not necessary to load a cocatalyst onto BWO. Such multielectron O_2 reduction can be driven even by metal-oxide photocatalysts having a lower CBB potential, such as tungstena, if they are loaded with noble-metal deposits for multielectron O_2 reduction [10], and the present BWO particles might be the first example for multielectron O_2 reduction by a pristine metal-oxide photocatalyst within the authors knowledge (Improbable one-electron oxygen reduction (and possible two-electron reduction) by BWO was suggested previously on the basis of the calculated/estimated CBB position without any experimental evidence [43,44].). Since it is practically impossible for metal oxides to reduce the band gap for visible-light absorption keeping the CBB potential higher (more cathodic) than SEP of one-electron oxygen reduction and multielectron O_2 reduction requires a lower CBB potential than the usual one-electron oxygen reduction does,

activation of smaller band-gap metal oxides by giving them multielectron O_2-reduction ability is a good strategy for the design and development of an efficient visible light-sensitive photocatalyst for POD.

Acknowledgements

FE-SEM analyses of samples were carried out using JEOL JSM-7400F and JSM-6360LA electron microscopes at the Open Facility, Hokkaido University Sousei Hall. This work was partly supported by Grant-in-Aid for Challenging Exploratory Research (KAKENHI) from the Japan Society for the Promotion of Science (JSPS) (16K1408606).

References

[1] K. Nakata, A. Fujishima, J. Photochem. Photobiol. C Photochem. Rev. 13 (2012) 169–189.
[2] V. Augugliaro, M. Bellardita, V. Loddo, G. Palmisano, L. Palmisano, S. Yurdakal, J. Photochem. Photobiol. C Photochem. Rev. 13 (2012) 224–245.
[3] T. Ochiai, A. Fujishima, J. Photochem. Photobiol. C Photochem. Rev. 13 (2012) 247–262.
[4] S. Kato and F. Masuo, Kogyo Kagaku Zasshi, 67, 42 (1964).
[5] J. Schwitzgebel, J. G. Ekerdt, H. Gerischer and A. Heller, J. Phys. Chem. 99 (1995) 5633–5638.
[6] T. Torimoto, Y. Aburakawa, Y. Kawahara, S. Ikeda, B. Ohtani, Chem. Phys. Lett. 392 (2004) 220–224.
[7] B. Ohtani, Y. Nohara and R. Abe, Electrochemistry 76 (2008) 147–149.
[8] B. Ohtani, Electrochemistry 82 (2014) 414–425.
[9] Y. Ohko, D. A. Tryk, K. Hashimoto and A. Fujishima, J. Phys. Chem. B, 102 (1998) 2699–2704.
[10] R. Abe, H. Takami, N. Murakami, B. Ohtani, J. Am. Chem. Soc. 130 (2008) 7780–7781.
[11] D. E. Scaife, Solar Energy 25 (1980) 41–54.
[12] L. Kavan, M. Grätzel, S. E. Gilbert, C. Klemenz, H. J. Scheel, J. Am. Chem. Soc. 118 (1996) 6716–6723.
[13] F. Amano, K. Nogami, R. Abe, B. Ohtani, J. Phys. Chem. C 112 (2008) 9320–9326.
[14] H. Hori, M. Takase, F. Amano, B. Ohtani, Chem. Lett. 44 (2015) 1723–1725.
[15] H. Hori, M. Takase, M. Takashima, F. Amano, T. Shibayama, B. Ohtani, Catal. Today in press.
[16] F. Amano, K. Nogami, B. Ohtani, Langmuir 26 (2010) 7174–7180.
[17] H. Hori, M. Takashima, M. Takase and B. Ohtani, Chem. Lett. 46 (2017) 1376-1378.
[18] F. Amano, K. Nogami, R. Abe and B. Ohtani, Chem. Lett. 36 (2007) 1314–1315.
[19] F. Amano, A. Yamakata, K. Nogami, M. Osawa and B. Ohtani, J. Am. Chem. Soc. 130 (2008) 17650–17651.
[20] B. Ohtani, Chem. Lett. 37 (2008) 217–229.
[21] F. Izumi and K. Momma, Solid State Phenom., 130 (2007) 15–20.

[22] H. Kominami, J.-i. Kato, M. Kohno, Y. Kera and B. Ohtani, Chem. Lett. 25 (1996) 1051–1052.
[23] H. Kominami, J.-i. Kato, S.-y. Murakami, Y. Kera, M. Inoue, T. Inui and B. Ohtani, J. Mol. Catal. A Chem. 144 (1999) 165-171.
[24] K. Nishijima, B. Ohtani, X. Yan, T.-a. Kamai, T. Chiyoya, T. Tsubota, N. Murakami and T. Ohno, Chem. Phys. 339 (2007) 64–72.
[25] S.-i. Nishimoto, B. Ohtani and T. Kagiya, J. Chem. Soc., Faraday Trans. 1 81 (1985) 2467–2474.
[26] H. Kominami, K. Oki, M. Kohno, S.-i. Onoue, Y. Kera and B. Ohtani, J. Mater. Chem. 11 (2001) 604–609.
[27] B. Ohtani, Y. Okugawa, S.-i. Nishimoto, T. Kagiya, J. Phys. Chem. 91 (1987) 3550–3555.
[28] O. Tomita, B. Ohtani and R. Abe, Catal. Sci. Tech. 4 (2014) 3850–3860.
[29] F. Amano, K. Nogami and B. Ohtani, J. Phys. Chem. C 113 (2009) 1536–1542.
[30] A. Kudo, S. Hijii, Chem. Lett. 28 (1999) 1103–1104.
[31] H. Fu, L. Zhang, W. Yao, Y. Zhu, Appl. Catal. B: Environ. 66 (2006) 100–110.
[32] R. Baba, S. Nakabayashi, A. Fujishima, K. Honda, J. Phys. Chem. 89 (1985) 1902–1905.
[33] B. Ohtani, K. Iwai, S.-i. Nishimoto, S. Sato, J. Phys. Chem. B. 101 (1997) 3349–3359.
[34] O.-O. Prieto-Mahaney, N. Murakami, R. Abe, B. Ohtani, Chem. Lett. 38 (2009) 238–239.
[35] B. Ohtani, O.-O. Prieto-Mahaney, F. Amano, N. Murakami, R. Abe, J. Adv. Oxidat. Tech. 13 (2010) 247–261.
[36] A. J. Bard, J. Phys. Chem. 86 (1982) 172–177.
[37] A. J. Bard, R. Parsons, J. Jordan, in Standard Potentials in Aqueous Solution, Marcel Dekker, New York and Basel, 1985.
[38] P. S. Rao, E. Hayon, J. Phys. Chem. 79 (1975) 397–402.
[39] F. Amano, M. Kitamura and B. Ohtani, unpublished results.
[40] S. Shiba, R. Ikeda, H. Remita-Bosi, B. Ohtani, E. Kowalska, to be submitted.
[41] G. M. Eisenberg, Ind. Eng. Chem. Anal. Ed., 15 (1943) 327–328.
[42] H. Hori, M. Takashima, M. Takase and B. Ohtani, to be submitted.
[43] T. Saison, P. Gras, N. Chemin, C. Chanéac, O. Durupthy, V. Brezová, C. Colbeau-Justin, J. -P. Jolivet, J. Phys. Chem. C 117 (2013) 22656–22666.
[44] J. Sheng, X. Li and Y Xu, ACS Catal. 4 (2014) 732−737.

Table 1 Physical/structural properties of BWO samples.

code	SSA[a] /m^2 g^{-1}	crystal- line form	crystal-linity (%)	NC[b] (%)	water (%)	D_{131}[c]/nm	t_{BWO}[d] /nm	V_p[e]/ cm^3 g^{-1}	
								HK	BJH
FB	20	russellite	83	17	1	17	14	0.9	0.9
WML	42	russellite	75	25	nd[h]	15	12	1.8	2.3
WMH	43	russellite	81	19	nd[h]	15	12	1.8	2.3
500FB	8	russellite	87	13	nd[h]	24	20	0.4	0.4
500WML	15	russellite	85	15	nd[h]	28	23	0.6	0.9
500WMH	15	russellite	81	19	nd[h]	28	23	0.6	0.8
Kojundo	3	(hexagonal)	86	14	nd[h]	–	–	nd[h]	nd[h]
Aldrich	1	(hexagonal)	51	49	nd[h]	–	–	nd[h]	nd[h]
FP-6	104	anatase	91	9	3	–	–	nd[h]	nd[h]
P25	58	anatase[g]	97	3	2	–	–	nd[h]	nd[h]
ST-G2	4	rutile	98	2	0.1	–	–	nd[h]	nd[h]
MT-150A	114	rutile	82	18	4	–	–	nd[h]	nd[h]

[a]Specific surface area. [b]Non-crystalline content. [c]Crystallite size calculated from 131 XRD peak. [d]Estimated thickness of BWO plates from D_{131}. [e]Total pore volume estimated using the HK or BJH method. [f]Estimated actual SSA. [g]Containing a small amount of rutile. [h]Not determined.

Table 2 Structural properties and photocatalytic activities of bismuth tungstate and bismuth molybdates prepared by HT and calcination [42] in CO_2, H_2 and O_2 systems.

code	composition	SSA[a] /m^2 g^{-1}	BG[b] /eV	activity[c]/μmol h^{-1}		
				CO_2	H_2	O_2
BWO-2	$Bi_2W_2O_9$	1	2.90	21	7	11
BMO-1	Bi_2MoO_6	4	2.65	8	0.03	6
BMO-2	$Bi_2Mo_2O_9$	2	2.66	25	< 0.01	2
BMO-3	$Bi_2Mo_3O_{12}$	1	2.58	12	< 0.01	1

[a]Specific surface area estimated from nitrogen adsorption at 77 K using the BET equation. [b]Band gap estimated from the absorption edge wavelength of diffuse reflectance spectra. [c]Photocatalytic activities in CO_2, H_2 and O_2 systems.

Figure captions

Fig. 1 FE-SEM images of (a, b) FB, (c) WML, (d) WMH, (e, f) 500FB, (g) 500WML and (h) 500WMH.

Fig. 2 XRD patterns of BWO samples.

Fig. 3 Pore-size distributions of BWO samples calculated using (a) the HK method and (b) BJH method.

Fig. 4 FE-SEM images of one-step platinized (a, b) FB, (c) WML, (d) WMH, (e, f) 500FB, (g) 500WML and (h) 500WMH and two-step platinized (i, j) FB, (k) WML, (l) WMH, (m, n) 500FB, (o) 500WML and (p) 500WMH.

Fig. 5 Diffuse reflectance spectra of (upper) neat BWO samples and (lower) BWO samples diluted (10%) with $BaSO_4$.

Fig. 6 Photocatalytic activities of BWO, tungstena and titania samples in (a) CO_2 (bare), (b) CO_2 (with loaded Pt), (c) H_2 (with loaded Pt) and (d) O_2 systems.

Fig. 7 Photocatalytic activities of (white) bare, (gray) one-step Pt-photodeposited and (black) two-step Pt-photodeposited BWO samples in the CO_2 system.

Fig. 8 Estimated conduction band-bottom (CBB) positions of anatase, rutile, tungstena and BWO and (standard) electrode potential as a function of pH.

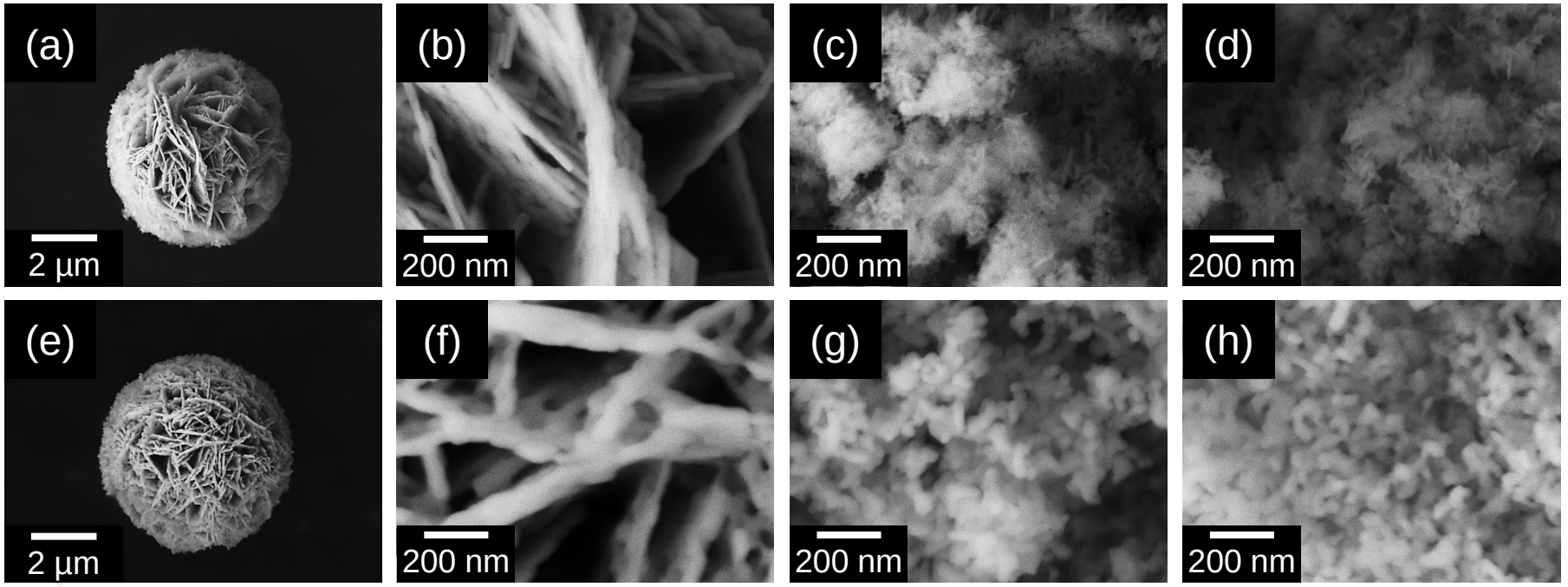

Fig. 1

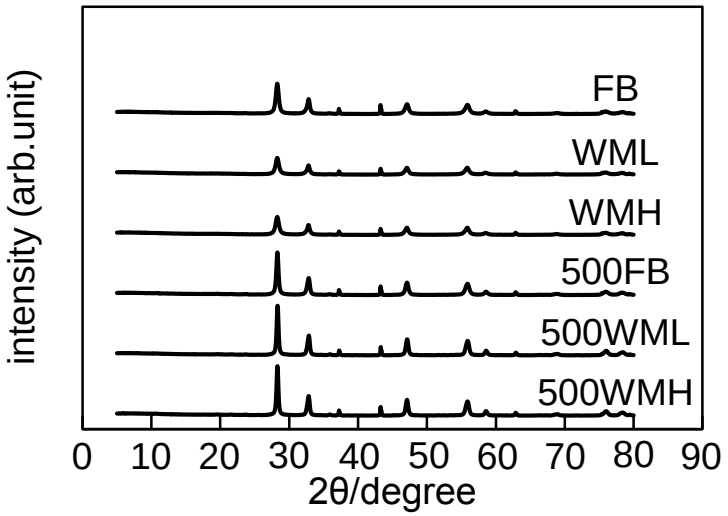
intensity (arb.unit)
FB
WML
WMH
500FB
500WML
500WMH
0
10
20
30
40
50
60
70
80
90
2θ/degree

Fig. 2

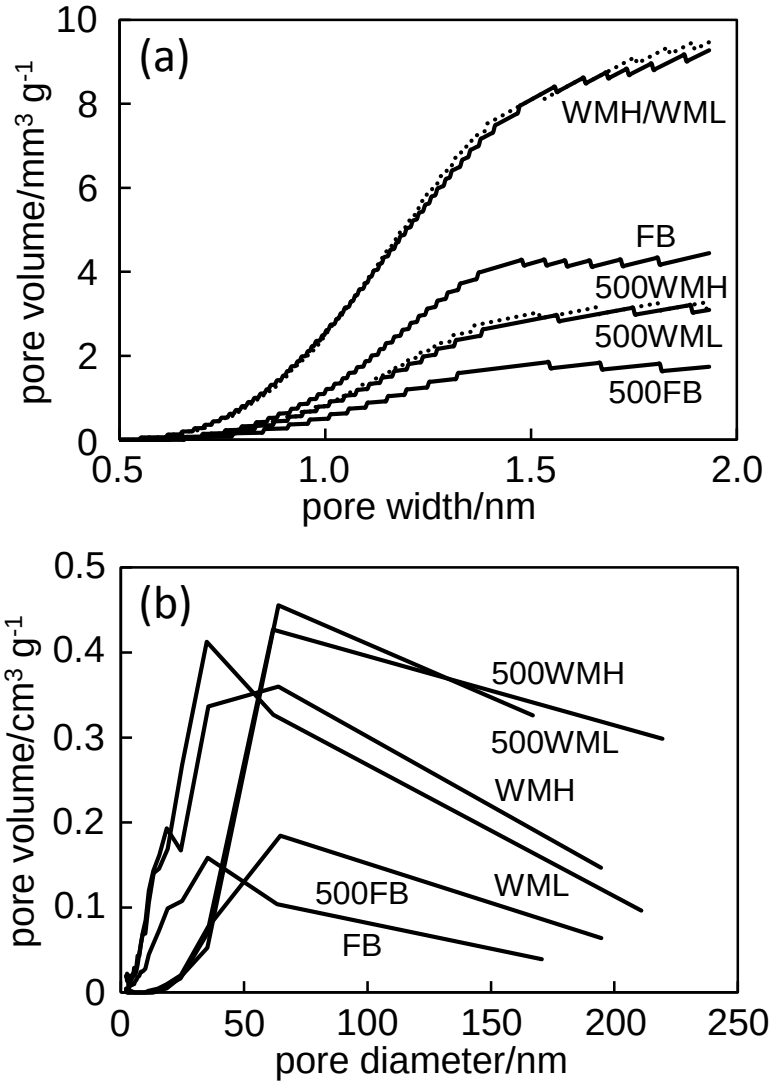
(a)
pore volume/mm^3 g^{-1}
pore width/nm
WMH/WML
FB
500WMH
500WML
500FB
(b)
pore volume/cm^3 g^{-1}
pore diameter/nm
500WMH
500WML
WMH
WML
500FB
FB

Fig. 3

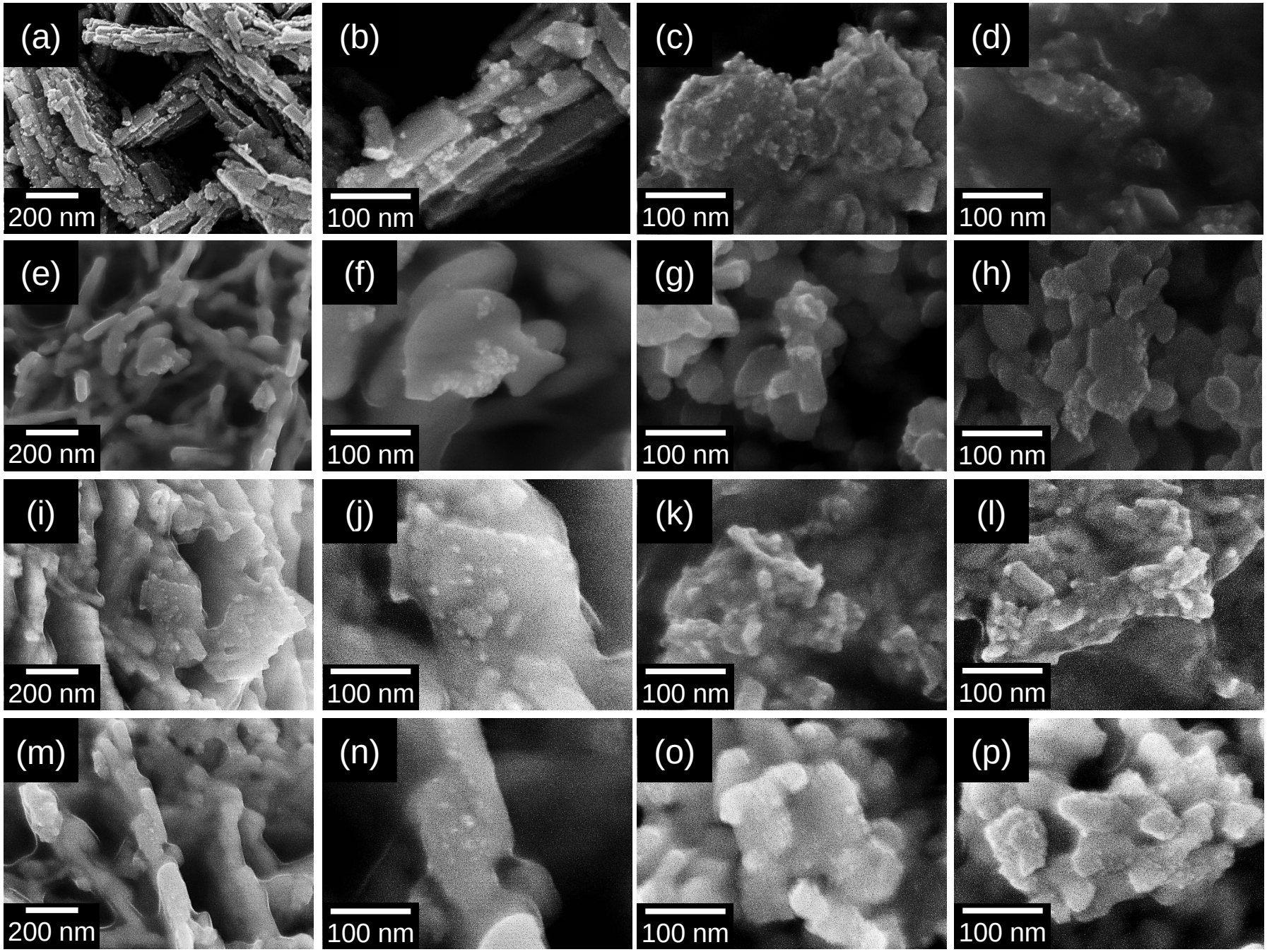
(a)
200 nm
(b)
100 nm
(c)
100 nm
(d)
100 nm
(e)
200 nm
(f)
100 nm
(g)
100 nm
(h)
100 nm
(i)
200 nm
(j)
100 nm
(k)
100 nm
(l)
100 nm
(m)
200 nm
(n)
100 nm
(o)
100 nm
(p)
100 nm

Fig. 4

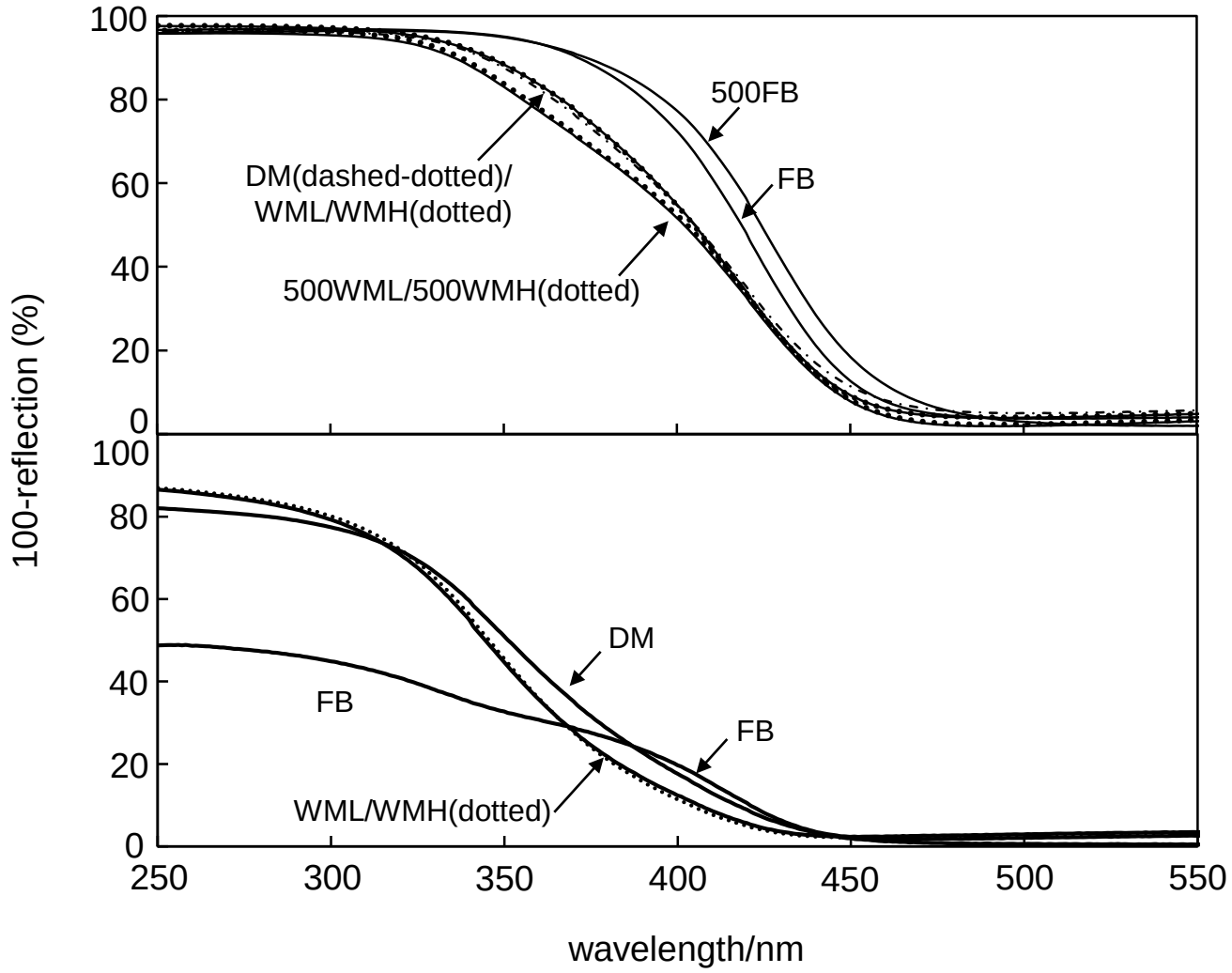
100-reflection (%)
100
80
60
40
20
0
500FB
FB
DM(dashed-dotted)/
WML/WMH(dotted)
500WML/500WMH(dotted)
DM
FB
FB
WML/WMH(dotted)
250
300
350
400
450
500
550
wavelength/nm

Fig. 5

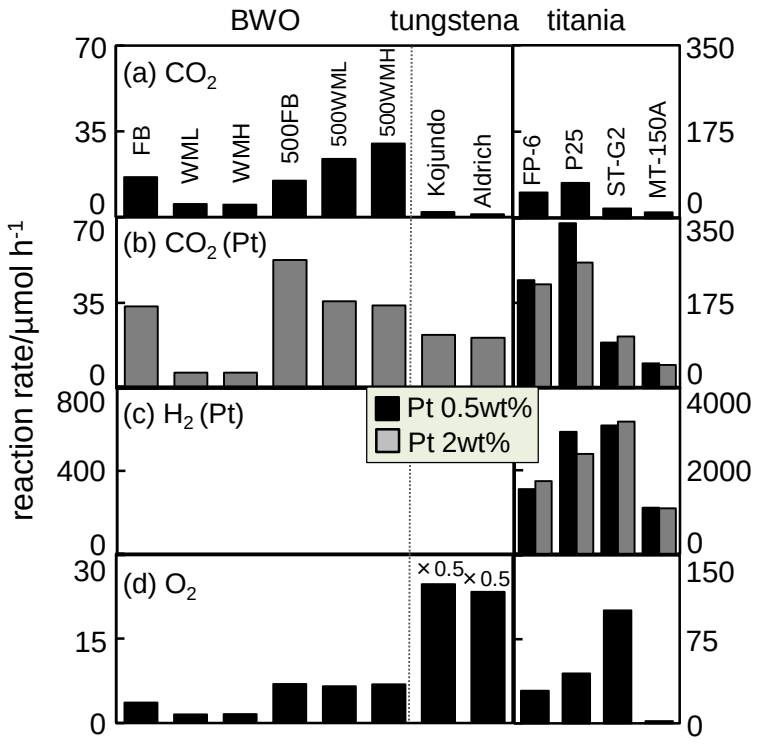
BWO
tungstena
titania
reaction rate/μmol h-1
(a) CO2
(b) CO2 (Pt)
(c) H2 (Pt)
(d) O2
FB
WML
WMH
500FB
500WML
500WMH
Kojundo
Aldrich
FP-6
P25
ST-G2
MT-150A
Pt 0.5wt%
Pt 2wt%
×0.5
×0.5
70
35
0
350
175
0
800
400
4000
2000
30
15
150
75

Fig. 6

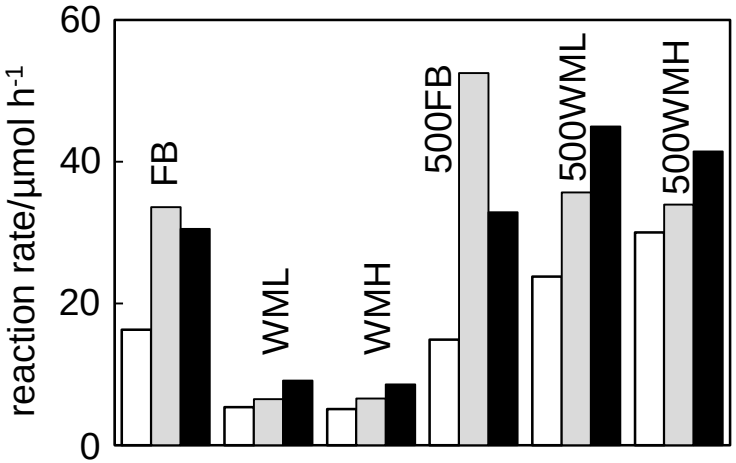
60
40
20
0
reaction rate/µmol h-1
FB
WML
WMH
500FB
500WML
500WMH

Fig. 7

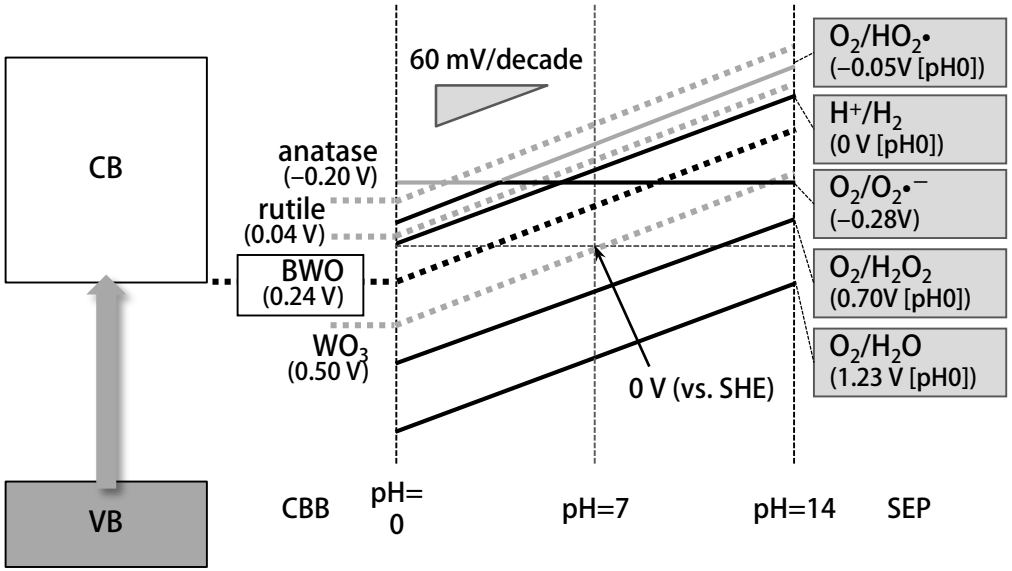
CB
VB
anatase
(−0.20 V)
rutile
(0.04 V)
BWO
(0.24 V)
WO3
(0.50 V)
60 mV/decade
0 V (vs. SHE)
O2/HO2•
(−0.05V [pH0])
H+/H2
(0 V [pH0])
O2/O2•−
(−0.28V)
O2/H2O2
(0.70V [pH0])
O2/H2O
(1.23 V [pH0])
CBB
pH=
0
pH=7
pH=14
SEP

Fig. 8